

MRI-Based Technique for Determining Nonuniform Deformations Throughout the Volume of Articular Cartilage Explants

C.P. Neu,¹ M.L. Hull,^{1,2*} J.H. Walton,³ and M.H. Buonocore⁴

Articular cartilage is critical to the normal function of diarthrodial joints. Despite the importance of the tissue and the prevalence of cartilage degeneration (e.g., osteoarthritis), the technology required to noninvasively describe nonuniform deformations throughout the volume of the tissue has not been available until recently. The objectives of the work reported in this paper were to 1) describe a noninvasive technique (termed the cartilage deformation by tag registration (CDTR) technique) to determine nonuniform deformations in articular cartilage explants with the use of specialized MRI tagging and image processing methods, 2) evaluate the strain error of the CDTR technique using a custom MRI-compatible phantom material, and 3) demonstrate the applicability of the CDTR technique to articular cartilage by determining 3D strain fields throughout the volume of a bovine articular cartilage explant. A custom MRI pulse sequence was designed to tag and image articular cartilage explants at 7 Tesla in undeformed and deformed states during the application of multiple load cycles. The custom pulse sequence incorporated the “delays alternating with nutations for tailored excitation” (DANTE) pulse sequence to apply tags. This was followed by a “fast spin echo” (FSE) pulse sequence to create images of the tags. The error analysis using the phantom material indicated that deformations can be determined with an error, defined as the strain precision, better than 0.83% strain. When this technique was applied to a single articular cartilage explant loaded in unconfined compression, heterogeneous deformations throughout the volume of the tissue were evident. This technique potentially can be applied to determine normal cartilage deformations, analyze degenerated cartilage, and evaluate cartilage surgical repair and treatment methodologies. In addition, this technique may be applied to other soft tissues that can be appropriately imaged by MR. Magn Reson Med 53: 321–328, 2005. © 2005 Wiley-Liss, Inc.

Key words: cartilage; MRI; deformation; strain; three-dimensional

Although articular cartilage has unique mechanical and tribological properties that allow for locomotion by providing a nearly frictionless and wear-resistant load-bearing

joint surface over an extended period of time, these properties can deteriorate, particularly in the elderly, resulting in the development of osteoarthritis. Osteoarthritis is a debilitating disease that affects 10% of Americans, and is associated with various degrees of cartilage degradation and altered joint load-deformation behavior (1). To improve our understanding of normal cartilage load-deformation behavior, as well as our ability to completely characterize, diagnose, and treat cartilage disorders such as osteoarthritis, it would be advantageous to determine the nonuniform mechanical deformations in response to applied loads throughout the volume of the tissue using noninvasive experimental methods. Hereafter, nonuniform deformation is termed “three-dimensional” (3D) deformation.

Methods to determine tissue deformation in response to applied loads are common in orthopedic research. Many previous investigations of soft biological tissue load-deformation behavior, such as that in cardiac (2) and meniscus (3) tissues, have employed invasive procedures to surgically expose and attach markers to directly track deformations. Noninvasive investigations of cardiac (4–6) and spinal cord (7) load-deformation behavior have employed MR tagging techniques to impose and then track features (typically a grid of tag lines) that deform with the tissue. Further noninvasive studies have combined MRI and texture correlation techniques to investigate intratendinous (8) and meniscus (9) deformations. In articular cartilage, noninvasive studies have combined optical image acquisition and image correlation techniques using either fluorescently-labeled chondrocyte nuclei (10,11) or superimposed enamel markers (12) in two-dimensional (2D) strain analyses on the imaging surface. Recently, an investigation of cartilage load-deformation behavior using MRI noninvasively quantified 2D strain in cartilage (13). Cartilage 3D surface deformation and volume changes in compression have also been documented by MRI (14,15). However, the results from these studies did not completely characterize 3D cartilage deformation, because changes in surface shape do not account for more complex behavior throughout the tissue volume (10,11). Thus, no study known to the authors has described a method to determine the 3D deformation throughout the volume of the tissue, although MR elastography methods have shown considerable promise for determining such detailed information in this small tissue (13,16–18).

Numerous challenges arise when one attempts to determine 3D cartilage deformations using MRI. Among these is the need to acquire high-spatial-resolution images to depict cartilage (from the tibial plateau) that is typically 1–2 mm thick in bovine tissue and <5 mm thick in human

¹Biomedical Engineering Graduate Group, University of California–Davis, Davis, California.

²Department of Mechanical Engineering, University of California–Davis, Davis, California.

³UC Davis Nuclear Magnetic Resonance Facility, University of California–Davis, Davis, California.

⁴Department of Radiology, University of California at Davis Medical Center, Sacramento, California.

Grant sponsor: National Science Foundation; Grant numbers: BES-0096436; OSTI 97-24412.

*Correspondence to: Maury L. Hull, Ph.D., Department of Mechanical and Aeronautical Engineering, University of California, One Shields Avenue, Davis, CA 95616. E-mail: mlhull@ucdavis.edu

Received 30 April 2004; revised 22 July 2004; accepted 26 August 2004.

DOI 10.1002/mrm.20343

Published online in Wiley InterScience (www.interscience.wiley.com).

© 2005 Wiley-Liss, Inc.

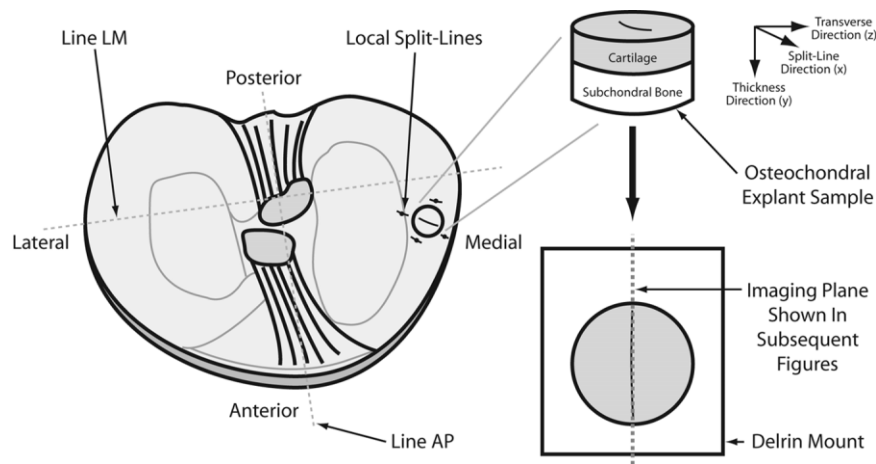


FIG. 1. Diagram showing the osteochondral explant harvested from the medial tibial plateau. The explant was secured to a Delrin mount and placed in a cyclic loading apparatus for deformation analyses. The imaging plane shown in subsequent figures was parallel to the local split-line direction of the explant. Compression was in the axial direction. Lines LM and AP were used to locate the explant.

tissue. Further, when MRI tagging techniques such as “delays alternating with nutations for tailored excitation” (DANTE) (19,20) are used, a high density (i.e., close spacing) of tag lines must be used to maximize trackable features. Temporal resolution also presents a fundamental challenge in determining 3D cartilage deformations. Unlike cardiac tissue, which has an intrinsic cyclic motion that enables MRI acquisition over many cycles, cartilage must be externally and cyclically loaded. The viscoelastic tissue must reach a steady-state load-displacement response prior to imaging (21).

The objectives of the work reported in this paper were threefold. The first was to describe a noninvasive technique (termed “cartilage deformation by tag registration” (CDTR)) to determine 3D deformations in articular cartilage explants with the use of specialized MRI tagging and image processing methods. The second objective was to evaluate the strain error of the CDTR technique using a custom MRI-compatible phantom material. The final objective was to demonstrate the applicability of the CDTR technique to articular cartilage by determining 3D strain fields throughout the volume of a bovine articular cartilage explant.

MATERIALS AND METHODS

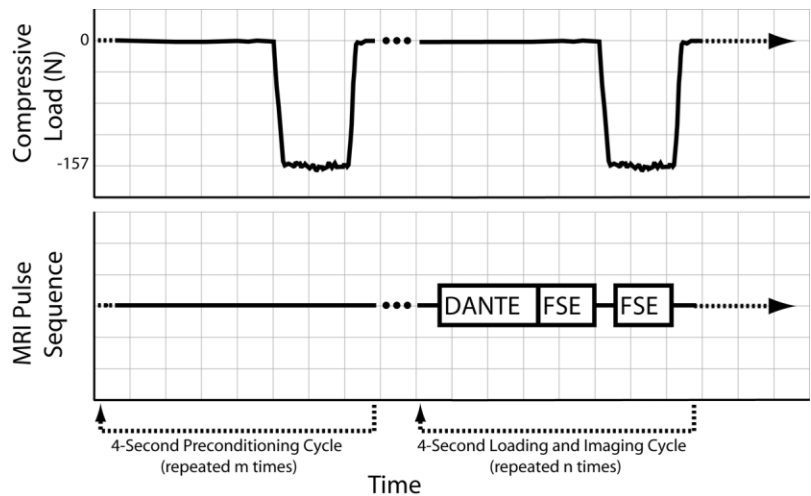
Our CDTR technique for determining articular cartilage deformation involved several primary steps: 1) image acquisition during material loading, 2) tag line identification and registration, and 3) deformation field spline fitting and strain calculation. Tags were generated, followed by image acquisition both before a cartilage explant was deformed by mechanical loading and after the cartilage explant was deformed (Fig. 1). Next, tag lines were superimposed on the images in both the undeformed and deformed states. Following tag line identification and registration from the undeformed and deformed image data, lines were fit by means of a B-spline model defined by control points. The model allowed us to locate any 3D material point within

the cartilage volume, and to perform subsequent 3D strain calculations at any point.

Image Acquisition During Material Loading

A custom MRI pulse sequence was designed to image articular cartilage explants in both undeformed and deformed states (Fig. 2). The pulse sequence incorporated DANTE and “fast spin echo” (FSE) pulse sequences. The DANTE sequence “tagged” or marked regions of cartilage that were subsequently tracked during tissue loading (20). The FSE sequence imaged the cartilage and tag lines in both undeformed and deformed states. The DANTE-FSE pulse sequence was used to image the cartilage on a Biospec 70/30 system (7.05 Tesla; Bruker Medical GmbH, Ettlingen, Germany) with microimaging gradients. The DANTE imaging parameters were as follows: radiofrequency (RF) pulses = 12; RF pulse angle = 15°; RF pulse duration = 8 μ s; interpulse duration = 400 μ s; magnetic field gradient strength along the cartilage explant axis = 17.5 Gauss/cm; and transverse magnetic field gradient strength = 10.0 Gauss/cm. The FSE imaging parameters were TR = 4000 ms; effective TE = 12.1 ms; number of echoes per excitation = 4; field of view = 15.3 \times 15.3 mm²; image matrix size = 256 \times 256 pixels²; number of averages = 4; and slice thickness = 1.0 mm. A 2D multislice set of images of 48 total images was acquired, with 24 images depicting undeformed cartilage, and 24 images depicting deformed cartilage. Of each group of 24 images, two sets of 12 images were acquired as orthogonal planes to allow for a 3D description of motion. These parameters resulted in multiple images with tag line spacings of 0.4 mm and 0.6 mm in the axial and transverse directions, respectively, and pixel dimensions of 60 \times 60 μ m² (Fig. 3). FSE proton density-weighted images resulted in minimal contrast between undeformed cartilage and the bathing solution. However, the deformation analyses described herein were accomplished using tag lines identified in undeformed and deformed images, and sufficient image contrast between the deformed cartilage and the solution.

FIG. 2. Timing diagram of the compressive loading and MRI pulse sequence actions. A number of preconditioning cycles were applied to the cartilage explants prior to MRI to reach a steady-state load-displacement response in the tissue and prevent motion artifacts in the images. The DANTE sequence applied a grid pattern of tag lines to the cartilage, while the FSE sequence acquired undeformed image data (prior to compressive loading) and deformed image data (during compressive loading).



The time available for FSE image acquisition was limited by the time duration of the tag lines superimposed by the DANTE pulse sequence. The contrast between the tag lines and the cartilage decayed according to the T_1 of the tissue (approximately 770 ms at 1.5 T, and >1000 ms at 7.05 T (22)). Imaging with this time constraint required an integration of the MRI scanner and the loading apparatus such that phase-encode steps were acquired over many loading cycles (Fig. 2). The loading apparatus consisted of electronic and pneumatic components, including a servo pressure regulator and double-acting cylinder such that load-controlled compression cycles were applied to cartilage explants with time-variable loading and recovery periods, and magnitude-variable applied normal stresses within typical physiological ranges (21). During each 4-s cycle, DANTE tag lines were applied to the tissue, and 12 undeformed phase-encode steps (four phase-encode steps from three different slices) were acquired. A mechanical compressive load of 157 N was then applied to the sample, followed by the acquisition of 12 deformed phase-encode steps. All imaging both before and during loading was performed in less than 800 ms, and the mechanical load was applied for a total of 1 s. To prevent blurring of images due to any changes in the deformation of the cartilage between load cycles, images were acquired only after the cartilage reached a steady-state load-displacement re-

sponse during the unconfined compressive cyclic loading applied by the loading apparatus (21). To ensure a steady-state deformation, 100 cyclic loads were applied prior to imaging. Subsequent to image acquisition, deformed images of cartilage (Fig. 3b) were segmented manually with the use of software employing closed Bezier curves to identify arbitrary object shapes within images (Paravision 3.0; Bruker Medical GmbH, Ettlingen, Germany) (Fig. 3c).

Tag Line Identification and Registration

Custom image processing software was written to determine 3D cartilage deformations in MATLAB (v.6.0, The Mathworks, Natick, MA). Active contours (23–25) were used to identify tag line locations in undeformed and deformed cartilage. We initially aligned a grid of active contours with tag lines in each image slice depicting undeformed cartilage by first summing pixel intensity values in row and column directions of the images, and then identifying rows and columns of minimum intensity. The number of active contours was ultimately chosen to enlarge the “region of interest” (ROI) around the cartilage such that spline fitting could describe deformation at the cartilage boundary (described below). A standard minimization algorithm was then applied to align contours with the undeformed DANTE grid (24,25). The algorithm al-

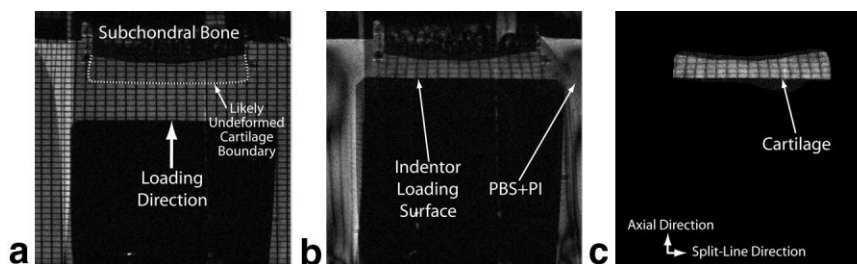


FIG. 3. Images depicting a single undeformed and deformed articular cartilage slice from the center of the 3D volume image. MR images of undeformed cartilage (a) were acquired with proton density-weighted contrast, and did not distinguish between the tissue and the bathing solution. Thus, cartilage and PBS+PI bathing solution occupy the space between the indenter surface and subchondral bone in (a). Motion of the indenter allowed for the deformed cartilage (b) to be clearly visualized and segmented (c). Considerable phase wrap occurred in the images, but the artifact did not interfere with the deformation analyses discussed herein.

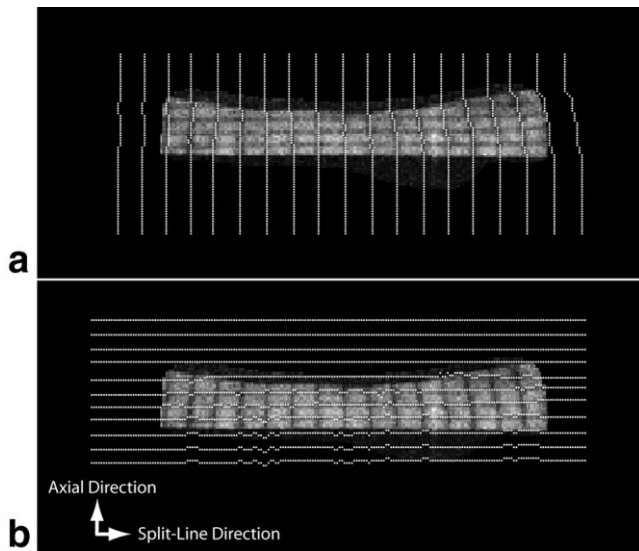


FIG. 4. Images depicting a single deformed articular cartilage slice from the center of the 3D volume image (Fig. 3c) with superimposed tag lines. The tag lines were extended outside the tissue to allow for deformation field spline fitting in x (a), y (b), and z (not shown).

lowed each tag line point to search pixel intensities in a neighborhood of points perpendicular to the original orientation of the tag line such that an energy functional for the contour was minimized. The tag lines were then placed on images depicting deformed cartilage, and minor user-interactive adjustments were made to initially align them with the deformed DANTE grid. The same minimization algorithm was then applied to align the contours with the deformed grid (Fig. 4). The segmented images of deformed cartilage were then thresholded, filled using binary dilation and erosion, and used as a binary image mask to exclude tag line points outside the cartilage boundary, because these point locations were affected by random image intensity noise near the tissue that was not completely eliminated during segmentation (Fig. 3c).

Deformation Field Spline Fitting and Strain Calculation

The ROI around the cartilage was enlarged to ultimately facilitate spline fitting of cartilage data at the tissue boundary (Fig. 4). For open cubic B-splines, this ROI was enlarged using at least two additional contours beyond the

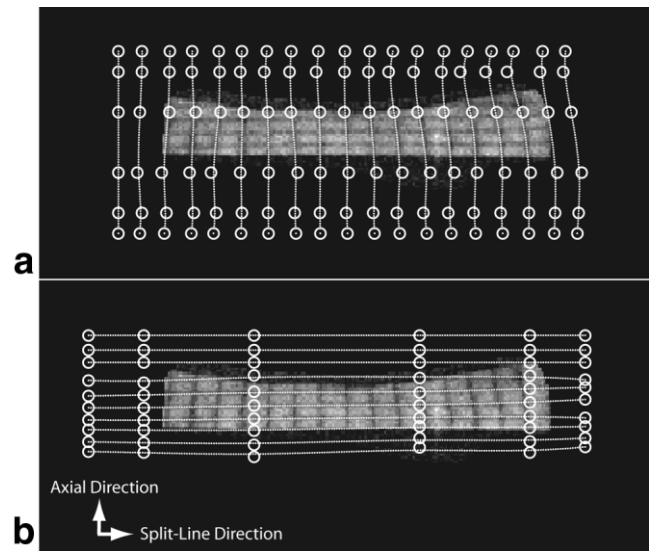


FIG. 6. Images depicting a single deformed articular cartilage slice from the center of the 3D volume image with superimposed control points and interpolated tag lines. The tag line data in x (a), y (b), and z (not shown) were parameterized using a B-spline fit in the respective directions. The direct correspondence between undeformed and deformed control points allowed for deformation (e.g., displacement and strain) field computations.

tissue boundary (26). Undeformed and deformed tag lines describing data in the subchondral bone were set equal to one another because negligible deformation occurred in this tissue for the given loading conditions. Other tag lines outside the cartilage boundary were given the same deformation of respective lines nearest to and within the tissue boundary. Additionally, the length of each tag line was extended to fill the ROI using the respective contour point location at the tissue boundary.

A B-spline model representation of all tag lines was obtained (Figs. 5 and 6). The model was governed by control points, and allowed for the interpolation of any undeformed or deformed location within the cartilage (26). Each tag line was fit to the B-spline model in a least-squares sense (27) with the use of six control points per line. Six control point arrays (corresponding to the three independent split-line (i.e., collagen fiber orientation on the articular surface), axial, and transverse directions described below, for each undeformed and deformed volume

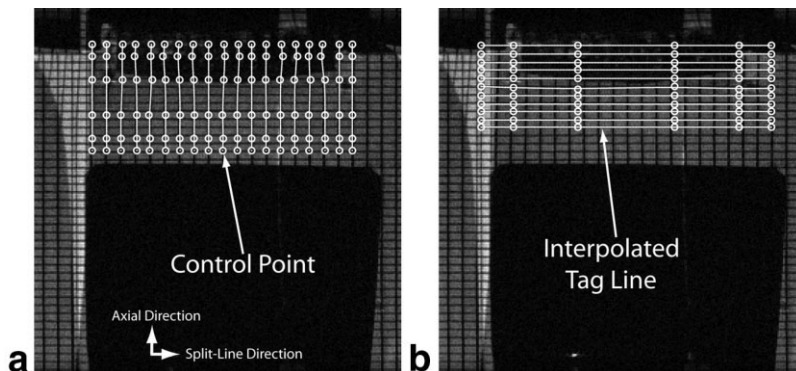


FIG. 5. Images depicting a single undeformed articular cartilage slice from the center of the 3D volume image with superimposed control points and interpolated tag lines. The tag line data in x (a), y (b), and z (not shown) were parameterized using a B-spline fit in the respective directions.

image) were assembled by means of B-spline fits of tag line data from multiple images. Finally, strain at each deformed pixel location inside the volume was determined using discrete data interpolated from control points describing material locations in undeformed and deformed states, and a maximum likelihood estimation of the deformation gradient tensor \mathbf{F} (28). The Green-Lagrange strain tensor \mathbf{E} was used to describe 3D strains at each deformed location:

$$\mathbf{E} = \frac{1}{2}(\mathbf{F}^T\mathbf{F} - \mathbf{I}) \quad [1]$$

where \mathbf{T} is the transpose, and \mathbf{I} is the identity tensor. Strain in the split line (E_{xx} ; see Application section below), axial (E_{yy}), and transverse (E_{zz}) directions, and shear strains (E_{xy} , E_{xz} , E_{yz}) were computed as a function of position directly as components of the Green-Lagrange strain tensor.

Error

An MRI-compatible phantom material was used to estimate the error for the entire technique. The phantom material was a silicone gel (Sylgard 527 dielectric gel; Dow Corning, Midland, MI) embedded with contrasting spherical markers (11 Delrin balls, 1.588 ± 0.051 mm diameter). The T_1 and T_2 properties of the gel were similar to those of articular cartilage (29) and occupied a volume of approximately $7 \times 7 \times 7$ mm³. A series of 10 repeated deformation experiments were performed on the phantom to estimate the strain error. Material loading for each experiment was configured for a 20-N cyclic load magnitude (for the soft gel) with a 1-s period of constant loading and a 3-s total cycle duration. Negligible deformation occurred in the stiff spheres (69 GPa modulus of elasticity (30)) compared to the soft silicone (2 MPa modulus of elasticity) under these loading conditions. The phantom material was imaged in undeformed and deformed states as described above for cartilage, except that the parameters were altered to obtain a spatial resolution of 100×100 μm^2 and a tag line spacing of approximately 1.0 mm. The B-spline model control points representing 3D phantom motion were found.

For each experiment, displacement error was determined as the difference between each deformed marker centroid location predicted using the deformation field spline fitting algorithm described herein, and the location measured directly using a software program (Scion Image 1.0; Scion Corporation, Frederick, MD) that allowed for a manual fit of a circle (to the spherical markers) in two orthogonal directions. The direct measurement of marker location represented the “gold standard,” with the location of the markers being identified to subpixel accuracy (31). The bias was defined as the mean displacement error for the 11 markers and 10 repeated experiments. A t-test was used to determine whether the bias was significantly different from zero. The strain was also determined at 27 locations (a $3 \times 3 \times 3$ array of points) distributed to characterize strain throughout the material. The absolute precision was defined as the standard deviation (SD) of the strain values (32) over the 10 repeated experiments. We

computed the SD by pooling the data for all six strain values at each of the 27 locations.

Studies in Bovine Articular Cartilage

The technique was demonstrated in a single bovine articular cartilage explant cyclically loaded in unconfined compression. An adult bovine knee joint was obtained from a local abattoir immediately following the death of the animal. The joint was disarticulated, and a cylindrical osteochondral explant was harvested from the medial tibial plateau beneath the medial meniscus (Fig. 1). The line LM was identified using the most lateral and medial points on the respective surfaces. The line AP was identified as perpendicular to LM and passing through the midpoint of the line connecting the tips of the tibial eminences. The explant was located in a medial direction along LM approximately 75% of the distance from the intersection of LM and AP to the most medial surface point. The explant was located in an anterior direction parallel to AP approximately 25% of the distance from the intersection of LM and AP to the most anterior surface point. A 10-mm-diameter coring reamer (AR-1224S; Arthrex, Naples, FL) was used to extract the explant, which consisted of cartilage (approximately 1–2 mm thick) and subchondral bone (approximately 2 mm thick). The articular surface was attached to a freezing stage (CryoHistomat; Hacker Instruments & Industries, Inc., Fairfield, NJ) and a circular saw and custom jig were used to remove subchondral bone and produce a surface parallel to the articular surface. During all harvesting procedures, phosphate-buffered saline with protease inhibitors (PBS+PI; 1 mM PMSF, 2 mM disodium EDTA, 5 mM benzamidine HCL, and 10 mM NEM (33)) was used to rinse and hydrate the cartilage. Additionally, the local split-line direction surrounding the explant was identified before it was removed from the tibia (34), and the direction was marked on the cartilage surface with India ink.

The explant was secured to a Delrin mount with ethyl cyanoacrylate and placed in the custom mechanism for cyclic loading in unconfined compression (21). Care was taken to align the split-line direction on the mount so that strain relative to the direction could be interpreted. During all of the experiments, PBS+PI was used to bathe the explant while it was inside the loading mechanism. All experiments were performed at room temperature. Although a 10-mm-diameter coring reamer was used, the explant measured 8.9 mm in diameter (as determined with calipers) after it was harvested. Thus, the 157 N load applied to the cartilage surface with a flat-surfaced and nonporous loading platen resulted in an applied normal stress of 2.53 MPa, which is within the physiological range during walking (35). After the cartilage was loaded by 100 cycles to reach steady-state cyclic deformation, the images were acquired and analyzed as described above, and the 3D strain fields in a single slice through the center of the tissue volume were determined (Fig. 1).

RESULTS

The bias in predicting deformed marker centroid locations was not significantly different from zero ($0.002 \pm$

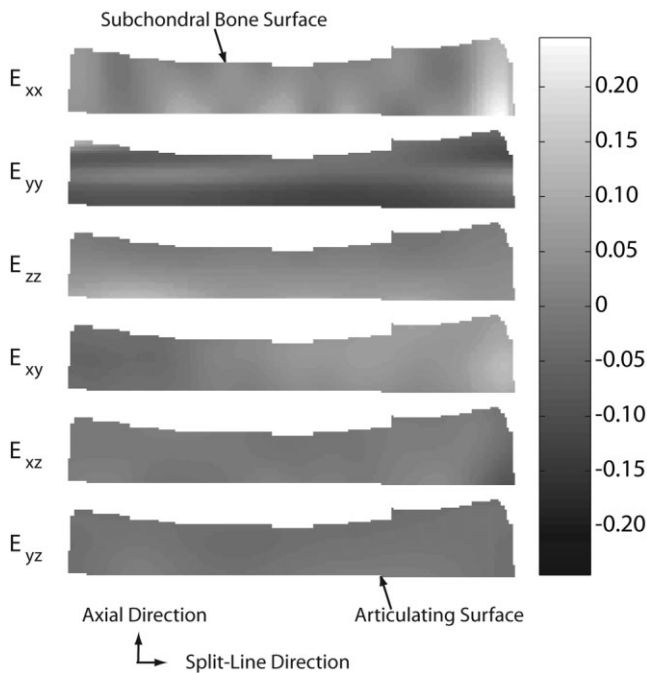


FIG. 7. 3D strain fields through a single deformed articular cartilage slice from the center of the 3D volume image. In-plane (E_{xx} , E_{yy} , and E_{xy}) and through-plane (E_{zz} , E_{xz} , E_{yz}) strains exhibit complex and heterogeneous patterns.

0.046 mm, $p = 0.854$). The absolute precision in determining strains was 0.83%. For strains as large as 25% observed in the sample under these loading conditions (discussed below), this absolute strain precision corresponds to a relative strain precision (i.e., absolute strain precision/mean strain) of 3.32%.

In the cartilage explant, an applied normal stress of 2.53 MPa during simple unconfined compression resulted in complex and heterogeneous 3D strains that approached 25% in some regions (Fig. 7). Throughout the tissue, strain in the axial direction (E_{yy}) was compressive, and at the center of the sample the strain magnitude increased nonlinearly with distance from the subchondral bone. Strains in both the split-line (E_{xx}) and transverse (E_{zz}) directions were tensile and varied throughout the tissue (with noticeably more heterogeneous patterns in the E_{xx} direction through this image slice). Consistent with these observations, strain in the E_{xy} direction also exhibited noticeable heterogeneous patterns, while strains in the E_{xz} and E_{yz} directions were more homogeneous.

DISCUSSION

This work demonstrates an MRI-based CDTR technique for determining 3D deformations throughout the volume of articular cartilage explants. In contrast to previous studies in which MRI tagging techniques were used to determine cardiac tissue deformation (4–6,36), in the present work the application of such techniques to cartilage deformations overcame two primary experimental challenges. First, cartilage was deformed with the use of a cyclic loading apparatus to enable 3D MR image acquisition over

large (>1 TR) time periods. Second, a sufficient tag line grid density was created to observe characteristic and representative deformations throughout the cartilage.

Although the use of the open cubic B-spline model provided a computationally useful representation of tissue motion, an accurate description of motion nearest the tissue boundary required some assumption about tag line data outside the tissue boundary. An ROI was initially defined to extend beyond the cartilage boundary (Fig. 3). As a result, strain at the free boundaries (i.e., those that were not attached to bone) was estimated based on the extrapolation of tag line data closest to the boundary. Alternative interpolation techniques (e.g., Hermite interpolation) would provide a more accurate description of motion at the free boundaries, provided the boundaries could be identified in undeformed and deformed images. However, it was not computationally possible to perform such an interpolation with the current technique, because image contrast was not adjusted to allow for high contrast between undeformed cartilage and the PBS+PI bathing solution. In the present work, standard spin-echo experiments were used to estimate properties for cartilage ($T_1 = 1479$ ms; $T_2 = 79$ ms; relative proton density = 0.89) and solution ($T_1 = 1427$ ms; $T_2 = 725$ ms; relative proton density = 1.00). Although improved contrast between the cartilage and the PBS+PI solution could have been obtained in images with heavy T_2 -weighting (at the expense of a lower cartilage signal), the data were acquired with proton density-weighted contrast. However, images of deformed cartilage depicted sufficient contrast between cartilage and the PBS+PI solution (Fig. 2b). This contrast, highlighted by the PBS+PI solution with missing DANTE tag lines, was due to indenter motion that caused mixing of the solution, and thus image intensities. Finally, the use of recent displacement-encoded MRI techniques (13,16–18) may obviate the need for extrapolation in determining strain at tissue boundaries.

Error was evaluated with the use of a custom MRI-compatible phantom material. The locations of spherical markers, which were embedded in the silicone gel and used to determine the bias of the technique, were calculated at subpixel resolution. In our study, 232 pixels defining a circle (our “gold standard”) were used to manually fit marker boundaries and determine the location of marker centroids with an error on the order of 3 μm (31) for each of the independent directions. Further, because the bias was not significantly different from zero (0.002 ± 0.046 mm, $p = 0.854$), it is reasonable to conclude that the propagation of this bias resulted in negligible strain bias. Thus, the error for the technique was random and was quantified by the strain precision determined in repeated observations. The 0.83% absolute strain precision was determined for MR images acquired at $100 \times 100 \mu\text{m}^2$. Acquisition at this spatial resolution was necessary to result in experiment times of reasonable duration (which would have exceeded 20 hr for 10 repeated measures of MR volume images acquired at $60 \times 60 \mu\text{m}^2$). The 0.83% strain precision represents an upper bound, because it is likely that the strain precision is inversely related to pixel size. Additionally, it is reasonable to expect that a negligible strain bias resulted from water permeation during mechanical loading, which was estimated to be less than 1 μm

(and negligible compared to the pixel width of 60 μm) based on permeability experiments of articular cartilage (33).

In comparing this error with that of other techniques for quantifying tissue deformation, a study of swelling-induced residual 2D cartilage strains estimated an accuracy of strain measurements at 0.20% using a combined optical image acquisition and image correlation technique (12). In an MRI and texture correlation study of intratissue deformation, a numerical propagation of displacement error estimated strain error of 0.68% at a 5% strain level (8). Another technique that used video microscopy and digital image correlation to measure 2D cartilage strain during compression reported tissue displacements with a 0.25–0.30 pixel measurement uncertainty, and deformation gradients (from which the strains are determined) with a 0.017–0.032 (dimensionless) measurement uncertainty without spline smoothing and differentiation, although the propagation of these uncertainties to strain uncertainty was not given (11). Thus, the error result from the present work compares most closely with that reported by Bey et al. (8).

The cartilage deformations presented here were complex and heterogeneous throughout the volume of the tissue. In the center of the sample, the deformation pattern was similar to those reported in studies using optical image acquisition and image correlation techniques (10,11), in that the axial strain (E_{yy}) increased with distance from the subchondral bone. This corresponds to decreased stiffness in the compressive modulus from the subchondral bone. However, more detailed comparisons are not warranted because the objective of the present work was to demonstrate our method through the use of a single cartilage explant.

Because our CDTR technique determines complex deformation fields (e.g., displacements and strains) at any point within the tissue volume, it has a number of possible applications. For example, this technique can be used to refine theoretical and computational models of cartilage that incorporate material property anisotropies to predict heterogeneous strain patterns under various loading conditions (37–39). It can also be applied to numerous experimental problems in which 3D strain data throughout the tissue volume is of interest. For example, documenting changes in deformations during enzymatic degradation of cartilage (33) may provide insights into the mechanisms of osteoarthritis. In a previous study, a canine anterior cruciate ligament transection model of osteoarthritis (40) documented a significant intrinsic moduli decrease in compression (24% of control values), tension (64%), and shear (24%) at 12 weeks after the surgery. Assuming a linear (i.e., Hookean) relationship between stress and strain, as well as a fixed applied stress in experimental tests, it is reasonable to expect that the 0.83% absolute strain precision is sufficient to document changes in strain (corresponding to reduced moduli) during the degenerative progression of osteoarthritis. Further, this technique potentially can be extended to whole joints for in vivo 3D cartilage deformation studies. Such an extension would require a determination of the loading cycles that are necessary to reach a steady-state load-displacement response in the tissues of whole legs, as well as the appropriate

pulse sequences for high-resolution studies in the clinical setting.

ACKNOWLEDGMENTS

The authors thank Prof. Marc Geers, Eindhoven University of Technology, The Netherlands, for providing his custom strain measurement code, and Laura Melton for her assistance in harvesting the cartilage explant.

REFERENCES

- Setton LA, Elliott DM, Mow VC. Altered mechanics of cartilage with osteoarthritis: human osteoarthritis and an experimental model of joint degeneration. *Osteoarthritis Cartilage* 1999;7:2–14.
- Waldman LK, Fung YC, Covell JW. Transmural myocardial deformation in the canine left ventricle. Normal in vivo three-dimensional finite strains. *Circ Res* 1985;57:152–163.
- Bylski-Austrow DI, Ciarelli MJ, Kayner DC, Matthews LS, Goldstein SA. Displacements of the menisci under joint load: an in vitro study in human knees. *J Biomech* 1994;27:421–431.
- Zerhouni EA, Parish DM, Rogers WJ, Yang A, Shapiro EP. Human heart: tagging with MR imaging—a method for noninvasive assessment of myocardial motion. *Radiology* 1988;169:59–63.
- Axel L, Dougherty L. Heart wall motion: improved method of spatial modulation of magnetization for MR imaging. *Radiology* 1989;172:349–350.
- McVeigh ER. MRI of myocardial function: motion tracking techniques. *Magn Reson Imaging* 1996;14:137–150.
- Yuan Q, Dougherty L, Margulies SS. In vivo human cervical spinal cord deformation and displacement in flexion. *Spine* 1998;23:1677–1683.
- Bey MJ, Ramsey ML, Soslowky LJ. Intratendinous strain fields of the supraspinatus tendon: effect of a surgically created articular-surface rotator cuff tear. *J Shoulder Elbow Surg* 2002;11:562–569.
- Gilchrist CL, Xia Q, Setton LA, Hsu EW. A first-order texture correlation algorithm and image roughness parameter to quantify soft tissue deformation using MRI. In Proceedings of the 2003 Summer BioEngineering Conference, Key Biscayne, FL, 2003.
- Schinagl RM, Ting MK, Price JH, Sah RL. Video microscopy to quantify the inhomogeneous equilibrium strain within articular cartilage during confined compression. *Ann Biomed Eng* 1996;24:500–512.
- Wang CC, Deng JM, Ateshian GA, Hung CT. An automated approach for direct measurement of two-dimensional strain distributions within articular cartilage under unconfined compression. *J Biomech Eng* 2002;124:557–567.
- Narmoneva DA, Wang JY, Setton LA. Nonuniform swelling-induced residual strains in articular cartilage. *J Biomech* 1999;32:401–408.
- Ridler AC, Plewes DB, Henkelman RM. Measurement of cartilage's internal elastic properties using MR elastography. In: Proceedings of the 9th Annual Meeting of ISMRM, Glasgow, Scotland, 2001. p 39.
- Herberhold C, Stammberger T, Faber S, Putz R, Englmeier KH, Reiser M, Eckstein F. An MR-based technique for quantifying the deformation of articular cartilage during mechanical loading in an intact cadaver joint. *Magn Reson Med* 1998;39:843–850.
- Eckstien F, Lemberger B, Stammberger T, Englmeier KH, Reiser M. Patellar cartilage deformation in vivo after static versus dynamic loading. *J Biomech* 2000;33:819–825.
- Aletas AH, Balaban RS, Wen H. High-resolution strain analysis of the human heart with fast-DENSE. *J Magn Reson* 1999;140:41–57.
- Plewes DB, Bishop J, Samani A, Sciarretta J. Visualization and quantification of breast cancer biomechanical properties with magnetic resonance elastography. *Phys Med Biol* 2000;45:1591–1610.
- Steele DD, Chenevert TL, Skovoroda AR, Emelianov SY. Three-dimensional static displacement, stimulated echo NMR elasticity imaging. *Phys Med Biol* 2000;45:1633–1648.
- Morris GA, Freeman R. Selective excitation in Fourier transform nuclear magnetic resonance. *J Magn Reson* 1978;29:433–462.
- Mosher TJ, Smith MB. A DANTE tagging sequence for the evaluation of translational sample motion. *Magn Reson Med* 1990;15:334–339.
- Neu CP, Hull ML. Toward an MRI-based method to measure non-uniform cartilage deformation: an MRI-cyclic loading apparatus system and steady-state cyclic displacement of articular cartilage under compressive loading. *J Biomech Eng* 2003;125:180–188.

22. Duijvel SH, Ceckler TL, Ong K, Wen H, Jaffer FA, Chesnick SA, Balaban RS. Musculoskeletal MR imaging at 4 T and at 1.5 T: comparison of relaxation times and image contrast. *Radiology* 1995;196:551–555.
23. Kass M, Witkin A, Terzopoulos D. Snakes: active contour models. *Int J Comput Vision* 1988:321–331.
24. Williams DJ, Shah M. A fast algorithm for active contours and curvature estimation. *CVGIP: Image Understand* 1992;55:14–26.
25. Kumar S, Goldgof D. Automatic tracking of SPAMM grid and the estimation of deformation parameters from cardiac MR images. *IEEE Trans Med Imaging* 1994;13:122–132.
26. Mortenson ME. Geometric modeling. New York: John Wiley & Sons, Inc.; 1997.
27. Ozturk C, McVeigh ER. Four-dimensional B-spline based motion analysis of tagged MR images: introduction and in vivo validation. *Phys Med Biol* 2000;45:1683–1702.
28. Geers MGD, De Borst R, Brekelmans WAM. Computing strain fields from discrete displacement fields in 2D-solids. *Int J Solids Struct* 1996; 33:4293–4307.
29. Young AA, Axel L, Dougherty L, Bogen DK, Parenteau CS. Validation of tagging with MR imaging to estimate material deformation. *Radiology* 1993;188:101–108.
30. Callister WD. Materials science and engineering: an introduction. New York: John Wiley & Sons, Inc.; 1994.
31. Antaki JF. An experimental and theoretical model for the passive biomechanical properties of the intact heart. Vols. I and II. PhD Dissertation, Department of BioEngineering. Pittsburgh, PA: University of Pittsburgh; 1991.
32. Standard practice for use of the terms precision and bias in ASTM test methods. Vol. E177–90a. West Conshohocken, PA: ASTM International; 1996.
33. Frank EH, Grodzinsky AJ, Koob TJ, Eyre DR. Streaming potentials: a sensitive index of enzymatic degradation in articular cartilage. *J Orthop Res* 1987;5:497–508.
34. Bullough P, Goodfellow J. The significance of the fine structure of articular cartilage. *J Bone Joint Surg Br* 1968;50:852–857.
35. Donahue TL, Hull ML, Rashid MM, Jacobs CR. A finite element model of the human knee joint for the study of tibio-femoral contact. *J Biomech Eng* 2002;124:273–280.
36. de Crespigny AJ, Carpenter TA, Hall LD. Cardiac tagging in the rat using a DANTE sequence. *Magn Reson Med* 1991;21:151–156.
37. Mow VC, Kuei SC, Lai WM, Armstrong CG. Biphasic creep and stress relaxation of articular cartilage in compression? Theory and experiments. *J Biomech Eng* 1980;102:73–84.
38. Frank EH, Grodzinsky AJ. Cartilage electromechanics—II. A continuum model of cartilage electrokinetics and correlation with experiments. *J Biomech* 1987;20:629–639.
39. Soltz MA, Ateshian GA. A conewise linear elasticity mixture model for the analysis of tension-compression nonlinearity in articular cartilage. *J Biomech Eng* 2000;122:576–586.
40. Setton LA, Mow VC, Muller FJ, Pita JC, Howell DS. Mechanical properties of canine articular cartilage are significantly altered following transection of the anterior cruciate ligament. *J Orthop Res* 1994;12:451–463.